Dynamics of an [Fe₄S₄(SPh)₄]²⁻ cluster explored *via* IR, Raman, and nuclear resonance vibrational spectroscopy (NRVS)-analysis using ³⁶S substitution, DFT calculations, and empirical force fields†

Yuming Xiao,[a] Markos Koutmos,[d] David A. Case,*[c] Dimitri Coucouvanis,[d] Hongxin Wang[a,b] and Stephen P. Cramer*[a,b]

We have used four vibrational spectroscopies—FT-IR, FT-Raman, resonance Raman, and ⁵⁷Fe nuclear resonance vibrational spectroscopy (NRVS)—to study the normal modes of the Fe–S cluster in [(n-Bu)₄N]₂[Fe₄S₄(SPh)₄]. This [Fe₄S₄(SR)₄]²⁻ complex serves as a model for the clusters in 4Fe ferredoxins and high-potential iron proteins (HiPIPs). The IR spectra exhibited differences above and below the 243 K phase transition. Significant shifts with ³⁶S substitution into the bridging S positions were also observed. The NRVS results were in good agreement with the low temperature data from the conventional spectroscopies. The NRVS spectra were interpreted by normal mode analysis using optimized Urey–Bradley force fields (UBFF) as well as from DFT theory. For the UBFF calculations, the parameters were refined by comparing calculated and observed NRVS frequencies and intensities. The frequency shifts after ³⁶S substitution were used as an additional constraint. A D_{2d} symmetry Fe₄S₄S′₄ model could explain most of the observed frequencies, but a better match to the observed intensities was obtained when the ligand aromatic rings were included for a D_{2d} Fe₄S₄(SPh)₄ model. The best results were obtained using the low temperature structure without symmetry constraints. In addition to stretching and bending vibrations, low frequency modes between ~50 and 100 cm⁻¹ were observed. These modes, which have not been seen before, are interpreted as twisting motions with opposing sides of the cube rotating in opposite directions. In contrast with a recent paper on a related Fe₄S₄ cluster, we find no need to assign a large fraction of the low frequency NRVS intensity to 'rotational lattice modes'. We also reassign the 430 cm⁻¹ band as primarily an elongation of the thiophenolate ring, with ~10% terminal Fe–S stretch character. This study illustrates the benefits of combining NRVS with conventional Raman and IR analysis for characterization of Fe–S centers. DFT theory is shown to provide remarkable agreement with the experimental NRVS data. These results provide a reference point for the analysis of more complex Fe–S clusters in proteins.

Introduction

Cubane-like 4-iron 4-sulfur clusters are among the most frequently encountered protein prosthetic groups in biology.[1] Apart from their roles in electron transfer,[2] they are now known to serve as sensors,[3] as biosynthetic precursors,[4] in radical catalysis,[5] and as components of larger heterometallic active sites.[6,7] Phylogenetic trees based on [Fe₄S₄]ⁿ⁺ binding motifs can help understand the evolutionary relationships between different organisms,[8] and these clusters have even been invoked in the origins of life.[9] Better understanding of their physical and chemical properties would have an impact across a wide range of disciplines.
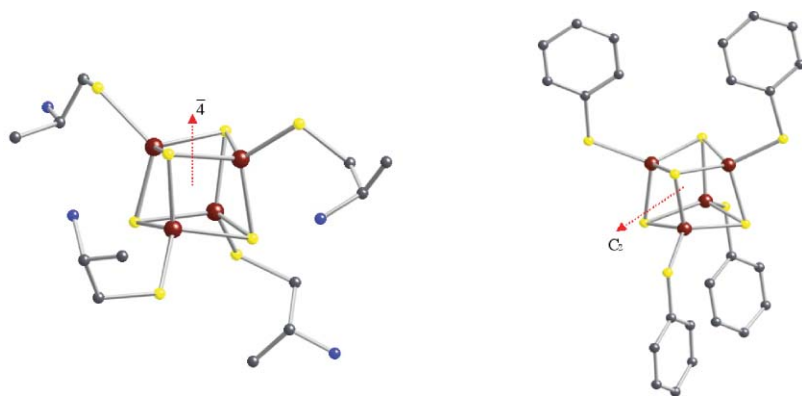
[a]*Department of Applied Science, University of California, Davis, CA 95616. E-mail: spcramer@ucdavis.edu, case@scripps.edu*
[b]*Physical Biosciences Division, Lawrence Berkeley National Laboratory, Berkeley, CA 94720*
[c]*Department of Molecular Biology, The Scripps Research Institute, La Jolla, CA 92037*
[d]*Department of Chemistry, University of Michigan, Ann Arbor, MI 48109*
† Electronic supplementary information (ESI) available: Fig. S1. See DOI: 10.1039/b513331a

High-resolution crystal structures are now available for several protein-bound [Fe₄S₄]²⁺ clusters at the 2+ oxidation level. For example, the [Fe₄S₄]²⁺ form of HiPIP from *Thermochromatium tepidum* has been studied at 0.8 Å resolution (1IUA),[10] *Bacillus thermoproteolyticus* ferredoxin has been interpreted at 0.92 Å (1IQZ),[11] and *Clostridium acidurici* ferredoxins have been probed at atomic (0.94 Å) resolution (1IQZ).[12] All of the [Fe₄S₄]²⁺ structures display approximately tetrahedral geometries, which are lowered to approximate D_{2d} symmetry *via* compression along an S₄ axis (Scheme 1).

A variety of low molecular weight synthetic model systems have been prepared as aids to understanding these clusters.[13] As with the protein-bound systems, the models are distorted from T_d symmetry in the solid state. For example, [Fe₄S₄(SCH₃)₄]²⁻ exhibits elongation of the S tetrahedron and compression of the Fe tetrahedron, both along the z-axis, which corresponds to the average direction of the S–C bonds.[14] This D_{2d} distortion results in 4 shorter Fe–S bonds and 8 slightly longer Fe–S bonds (Scheme 1). Based on changes in the Raman spectra in solution, it has been proposed that these distortions are solid state effects, and that in solution, the natural symmetry of the [Fe₄S₄(SR)₄]²⁻ clusters is

Scheme 1 Left—ball-and-stick model for the $[Fe_4S_4(Scys)_4]^{2-}$ cluster in *Bacillus thermoproteolyticus* ferredoxin, illustrating the principal 4 axis.[11] Right—the low temperature structure of the $[Fe_4S_4(SPh)_4]^{2-}$ cluster, illustrating the approximate C_2 axis.

T_d.[15] Others have argued that the distortion from T_d symmetry is a consequence of spin-coupling involving ferromagnetically coupled $S = 9/2$ pairs which are in turn coupled antiferromagnetically to give an $S = 0$ system.

The structure of the $[Fe_4S_4(SPh)_4]^{2-}$ cluster, which is the subject of the current investigation, has been known for 30 years,[16] and several more recent structures are also available.[17–19] The [(n-Bu)$_4$N]$_2$[Fe$_4$S$_4$(SPh)$_4$] salt undergoes a solid state phase transition at 243 K. Excoffon and coworkers have reported the structure of the orthorhombic 'phase I' at 233 K, comparing it with the monoclinic 'phase II' at 291 K.[19] In contrast with most $[Fe_4S_4(SR)_4]^{2-}$ clusters, they determined neither structure could be accurately described as T_d or even D_{2d}; the only symmetry they found was a C_2 axis for the low temperature cubane[19] (Scheme 1).

The dynamical properties of $[Fe_4S_4]^{n+}$ clusters may play an important role in their redox properties.[2] Our knowledge of cluster dynamics comes primarily from IR and Raman spectroscopy. The solution resonance Raman spectrum for $[Fe_4S_4(SPh)_4]^{2-}$ has been reported,[20] resonance Raman and FT-IR studies of $[Fe_4S_4(SCH_2Ph)_4]^{2-}$ were reported by Czernuszewicz *et al.*,[15] and the $[Fe_4S_4(SCH_3)_4]^{2-}$ analogue has been investigated by Kern and coworkers.[14] Spiro's group used a Urey–Bradley force field to successfully reproduce most of the Fe–S stretching mode frequencies,[15] and Kern and coworkers have elaborated a similar force field based on IR and Raman data for $[Fe_4S_4(SCH_3)_4]^{2-}$.[14] Although some bending modes were reported in the earlier papers, they have received relatively less attention in later studies, and these modes were not included in the more recent force field analysis.

Nuclear resonance vibrational spectroscopy (NRVS) is a relatively new technique for probing the vibrational properties of inorganic materials.[21,22] In the NRVS experiment, a monochromatic X-ray beam is scanned through the nuclear resonance. Along with the familiar 'zero phonon' (recoil-free) Mössbauer resonance, there are additional transitions that correspond to nuclear excitation combined with excitation (Stokes) or de-excitation (anti-Stokes) of vibrational modes. The NRVS method offers less restrictive selection rules than infrared or resonance Raman spectroscopy—on resonance the only requirement for NRVS intensity is motion of the resonant nucleus (in this case ^{57}Fe) along the direction of the incident X-ray beam in the given normal mode. The details of NRVS theory have been explained elsewhere;[22,23] the bottom line for the current study is that the one phonon NRVS excitation probability $S_1(\bar{\nu})$, is directly proportional to the Fe partial vibrational density of states (PVDOS) $D_{Fe}(\bar{\nu})$ and inversely proportional to $\bar{\nu}$:[24]

$$S_1(\bar{\nu}) = [\bar{n}(\bar{\nu}) + 1]\frac{\bar{\nu}_R}{\bar{\nu}}D_{Fe}(\bar{\nu}) \qquad (1)$$

where $\bar{\nu}$ is the difference between the photon energy and the recoil-free nuclear resonance energy (in wavenumbers), $\bar{\nu}_R$ is the recoil energy, $\bar{n} = [\exp(hc\bar{\nu}/k_BT) - 1]^{-1}$ is the thermal occupation factor for a mode of frequency $\bar{\nu}$ at temperature T.[23,25] The PVDOS function $D_{Fe}(\bar{\nu})$ arises from convolution of a lineshape function $L(\bar{\nu} - \bar{\nu}_a)$ with delta functions proportional to the Fe mode composition factor, e_{Fe}^2, for normal modes α at resonant energies $\bar{\nu}_a$. The iron PVDOS spectra can be extracted from the raw NRVS spectra using the PHOENIX software package,[26] and e_{Fe}^2 for a given eigenvector can be calculated from a normal mode analysis by:[23]

$$e_{Fe}^2 = \frac{m_{Fe}r_{Fe}^2}{\sum_j m_j r_j^2} \qquad (2)$$

where m_{Fe} and m_j refer to the masses of the Fe atom or other atom j, while r_{Fe} and r_j refer to the distance moved by Fe or other atom j, respectively.

In this paper we report ^{57}Fe NRVS for [(n-Bu)$_4$N]$_2$[$^{57}Fe_4S_4$(SPh)$_4$] with natural abundance sulfur as well as with ^{36}S substituted into the bridging sulfide positions. Resonance Raman, Fourier Transform Raman, and FT-IR spectra for this compound are presented to assist with the mode assignments. The spectra are compared with theoretically calculated ^{57}Fe PVDOS based on DFT calculations. Finally, normal mode calculations using an empirical UBFF in T_d, D_{2d}, C_2, and C_1 symmetry are used to reproduce and interpret the experimental spectra. The NRVS spectra contain information about both the frequency and the amplitude of iron motion, and they extend to lower frequencies than typical Raman spectra. By combining all of these data, we were able to refine a robust Urey–Bradley force field for this cluster. We could also clarify the assignment of several modes at low and high frequencies. The results are compared with previous IR and Raman based assignments and force fields.

Results and discussion

As Excoffon and coworkers have noted, the low temperature structure of the cluster $[(n\text{-Bu})_4N]_2[Fe_4S_4(SPh)_4]$ only has C_2 symmetry.[19] However, nearly all of the Fe_4S_4 cluster vibrational spectra have been assigned in D_{2d} symmetry. For reference, in Scheme 2 we include a modification of a diagram of Czernuszewicz and coworkers that illustrates the expected stretching modes.[15] In descending from T_d to D_{2d} symmetry, the T_1 modes split into A_2 and E modes, the T_2 modes split into B_2 and E modes, and the E modes into A_1 and B_1 modes:[20,27]

$$\Gamma_{vib} = 3A_1 + \underbrace{3A_1 + 3B_1}_{3E} + \underbrace{3A_2 + 3E}_{3T_1} + \underbrace{5B_2 + 5E}_{5T_2} \qquad (3)$$
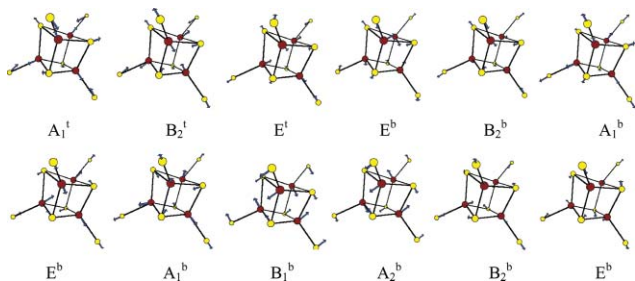
Scheme 2 Some normal modes of vibration and symmetry labels for a D_{2d} $Fe_4S^b_4S^t_4$ cluster. For the E modes, only one member of the degenerate pair is shown.

In D_{2d} symmetry, only the E and B_2 modes are IR-active, and the IR spectra can thus help with symmetry assignments. Although all of the modes are theoretically resonance Raman active, the A_1 modes are generally the strongest under resonance Raman conditions, and thus the Raman spectrum also gives clues as to the mode symmetries. Finally, since the splitting of T_2 modes into E and B_2 bands results from a small structural perturbation, their relative NRVS (and IR) intensities should be approximately 2 : 1, in accord with their relative degeneracy. This provides another clue in the symmetry assignments.

Isotope-dependent infrared spectra

In Fig. 1, IR spectra for $[(n\text{-Bu})_4N]_2[^{57}Fe_4S_4(SPh)_4]$ and $[(n\text{-Bu})_4N]_2[^{57}Fe_4{}^{36}S_4(SPh)_4]$ at 100 K are presented. For comparison, data are available for $(Et_4N)_2[Fe_4S_4(SCH_2Ph)_4]$[15] and $[(t\text{-Bu})_4N)]_2[Fe_4S_4(SMe)_4]$.[14] At 100 K, the strongest features for the ^{32}S sample involve a set of peaks at 382, 376, and 358 cm^{-1}, compared to peaks at 386, 366, and 359 cm^{-1} for $(Et_4N)_2[Fe_4S_4(SCH_2Ph)_4]$. In the $[(t\text{-Bu})_4N]_2[Fe_4S_4(SMe)_4]$ IR spectrum, an unresolved feature is seen at 355 cm^{-1}, while the higher frequency mode splits into two components at 384 and 388 cm^{-1}.[14] Both groups assign the lower frequency pair to components of a split T_2 Fe–S^t stretch and the higher energy modes as components of a split T_2 Fe–S^b stretch.[15] With ^{36}S substitution of the bridging sulfides, the 100 K $[^{57}Fe_4{}^{36}S_4(SPh)_4]$ peaks shift to 372, 356, and 345 cm^{-1}, indicating a significant component of bridging S motion in all of these modes.

In the 100 K natural abundance spectrum, additional strong bands are seen at ~288, 432, and 470 cm^{-1}; the latter has been attributed to a 'ligand' mode in $(Et_4N)_2[Fe_4S_4(SCH_2Ph)_4]$.[15] In
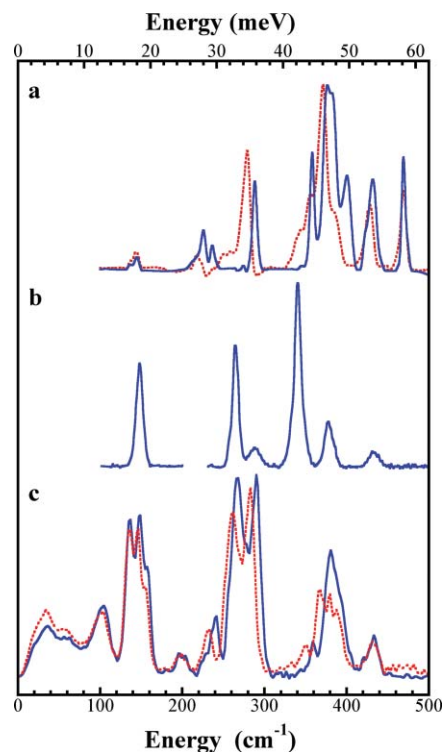
Fig. 1 Top to bottom: (a) FT-IR spectra at 100 K for $[(n\text{-Bu})_4N]_2$-$[^{57}Fe_4S_4(SPh)_4]$ (blue line) and $[(n\text{-Bu})_4N]_2[^{57}Fe_4{}^{36}S_4(SPh)_4]$ (red dashed line); (b) resonance Raman spectrum at 77 K for $[(n\text{-Bu})_4N]_2[^{57}Fe_4S_4(SPh)_4]$ with 4880 Å (blue line) excitation; (c) ^{57}Fe PVDOS spectra at 60 K for $[(n\text{-Bu})_4N]_2[^{57}Fe_4S_4(SPh)_4]$ (blue line) and $[(n\text{-Bu})_4N]_2[^{57}Fe_4{}^{36}S_4(SPh)_4]$ (red dashed line).

agreement with this assignment, the 470 cm^{-1} band is invariant with substitution of ^{36}S into the bridging positions. In contrast, the 288 cm^{-1} mode shifts to 279 cm^{-1} upon ^{36}S substitution. It therefore must have significant bridging S motion. In this region, Kern and coworkers assigned Raman features at 272 and 284 cm^{-1}, respectively, to A_2 and E modes derived from a T_1 Fe–S^b stretch, but as expected in D_{2d} symmetry, they observed negligible IR intensity.[14] Finally, the 432 cm^{-1} band downshifts only 3 cm^{-1} to 429 cm^{-1} with ^{36}S substitution. This mode therefore has relatively little motion of the bridging S; in fact, Moulis *et al.* assigned it to a Fe–S^t stretch.[20]

Resonance Raman spectra

The solid state resonance Raman spectrum for $[(n\text{-Bu})_4N]_2$-$[Fe_4S_4(SC_6H_5)_4]$ has not been reported, although a spectrum for the Et_4N^+ salt in acetonitrile solution is available.[20] For comparison with the NRVS, we therefore recorded Raman spectra for our $[(n\text{-Bu})_4N]_2[^{57}Fe_4S_4(SC_6H_5)_4]$ sample with 4880 Å excitation (Fig. 1). The strongest Raman feature is at ~340 cm^{-1}; previously, a 345 cm^{-1} band was observed in the natural abundance solution spectrum by Moulis and coworkers and assigned as an A_1 breathing mode involving mostly bridging S motion.[20] This A_1 mode is also the dominant band in the Raman spectra of the benzylthiolate[15] and methylthiolate[14] cubes, where it occurs at 335 cm^{-1} and 333 cm^{-1} respectively; the latter two analyses also concurred on the 'A_1^b' assignment.

The next strongest Raman mode with 4880 Å excitation is seen at ~264 cm^{-1} (Fig. 1). This feature presumably corresponds to the 276 cm^{-1} mode assigned as A$_1$ in the solution spectrum.[20] In other analyses,[14,15] there are no A$_1$ assignments in this region; instead, bands at ~270 and ~283 are assigned, respectively, as A$_2$ and E (or *vice versa*) modes derived from the T$_1$ Fe–S$_b$ stretch. We observe a much weaker Raman mode at ~290 cm^{-1} that is also evident in the solution spectrum.[20] Moulis and coworkers assigned this feature as B$_2$/E symmetry derived from a tetrahedral T$_2$ mode. It presumably corresponds with a band at 298 cm^{-1} in the solid state (Et$_4$N)$_2$[Fe$_4$S$_4$(SCH$_2$Ph)$_4$] spectrum. In this case the band was assigned as A$_1$, derived from the A$_1$/B$_1$ splitting of a tetrahedral E mode in D$_{2d}$ symmetry.[15] The disappearance of the latter mode upon dissolving [Fe$_4$S$_4$(SCH$_2$Ph)$_4$]$^{2-}$ in acetonitrile was taken as evidence for a D$_{2d}$ → T$_d$ transformation in solution.[15]

In the low energy range, a strong band is seen at ~147 cm^{-1} (Fig. 1). This can be compared with a peak at 145 cm^{-1} in both the [Fe$_4$S$_4$(SPh)$_4$]$^{2-}$ solution spectrum and for frozen *Cp* ferredoxin.[20] Kern *et al.* assigned a similar band at 152 cm^{-1} in [Fe$_4$S$_4$Cl$_4$]$^{2-}$ as the 'A$_1^{Fe}$' mode- a 'breathing vibration of the cluster primarily involving metal motion'.[28] In contrast, Czernuszewicz and coworkers assigned the breathing modes at 165 cm^{-1} for the benzyl cube and *Cp* ferredoxin.[15] The FT-Raman spectrum exhibits another low energy band at ~120 cm^{-1}; a similar band at ~122 cm^{-1} was observed in the [Fe$_4$S$_4$(SCH$_3$)$_4$]$^{2-}$ spectrum.

At the high frequency end, a broad band at 433 cm^{-1} is seen with 4880 Å excitation. A band at 435 cm^{-1} band is the strongest feature in the solution spectrum with 4579 Å excitation; this was assigned as an A$_1$ totally symmetric Fe–S$_t$ stretch.[20] For [Fe$_4$S$_4$(SPh)$_4$]$^{2-}$[20] and [Fe$_4$S$_4$(SCH$_2$Ph)$_4$]$^{2-}$,[15] bands associated with the aromatic ligand have also been reported in the 470–480 cm^{-1} region. None of the ferredoxins seem to have cluster-based fundamentals above 400 cm^{-1}. As will be shown below, the NRVS spectra are extremely useful for clarifying these assignments.

NRVS PVDOS Spectra

The ^{57}Fe PVDOS spectra for [(n-Bu)$_4$N]$_2$[^{57}Fe$_4$S$_4$(SC$_6$H$_5$)$_4$] and [(n-Bu)$_4$N]$_2$[^{57}Fe$_4$^{36}S$_4$(SC$_6$H$_5$)$_4$] are compared in Fig. 1. Three major features are observed in the [(n-Bu)$_4$N]$_2$[^{57}Fe$_4$S$_4$(SC$_6$H$_5$)$_4$] PVDOS spectra—a broad band near 381 cm^{-1}, a doublet at 267/290 cm^{-1} and a triplet at 137/148/157 cm^{-1}. The weaker features are summarized in Table 1. Apart from a minor peak at 200 cm^{-1}, there is a clear gap between the modes that are primarily Fe–S stretch in character, and those below 200 cm^{-1} that derive primarily from bending and torsional motions.

In the spectra for the ^{36}S-labeled sample, there are frequency shifts for most of the features above 200 and below 400 cm^{-1}, while the remaining bands change relatively little. The modes with large fractional shifts have a large percentage of Fe–S$_b$ stretch character.

Table 1 Summary of Raman, IR, NRVS spectra and normal mode analyses for (NEt$_4$)$_2$[Fe$_4$S$_4$(SPh)$_4$] and (NEt$_4$)$_2$[Fe$_4$^{36}S$_4$(SPh)$_4$][a]

Mode	Symmetry	Frequency/cm^{-1}				Frequency/cm^{-1}			
		Raman	IR	NRVS	calc	Raman	IR	NRVS	calc
	A$_1$		—		430.4				430.4
Ligand + Fe–S^t stretch	E	433 u	432	433 u	429.3		429 u	433 u	429.2
	B$_2$	435 m	426s		429.1				429.0
Fe–S^t stretch	A$_1$	382 u	—	395 s, u	390.4		—	388 u	390.1
mixed Fe–S stretch	B$_2$		400		388.3		386		386.1
	E		382s	381 u	380.8		372	380	380.8
mostly Fe–S^b stretch	E		376		378.6		356	367	364.6
	B$_2$	368 m	358	360	361.0		345	350	349.5
Fe–S^b stretch	A$_1$	340 345 m	—	344 vw	347.1		—	333 vw	332.9
	E		288		294.0		279		288.8
Fe–S^b stretch	A$_1$	290 293 m	—		299.9				295.5
	B$_1$			290 u	286.2			283 u	277.5
	A$_2$				278.4				269.2
	B$_2$		276w		284.1				281.5
	A$_1$	264 276 m			268.5			261 u	262.2
	E	265 m	264 vw	256 s	266.1		250 s 259 w		258.9
	E		237	240	236.4			232	229.3
	B$_2$	226	226 s	221.1		218	220 s	213.4
	B$_1$			~199 b	197.3			~199 b	193.4
	A$_2$				176.6				174.1
S–Fe–S′ bend	A$_1$				179.0			170 vw	176.9
	E		157	157.2			155	154.3
	A$_1$	147 145 m	148	143.7			146	140.7
	E		145	137 u	141.4		143	136	139.3
	B$_2$		136		131.4		137		129.8
	B$_2$			103 b	101.8			101 b	100.7
	E				90.7				90.3
	A$_1$			~60 u	55.3			~60 u	55.2
cubane twist	B$_1$				54.3				53.9
	E			~36	39.4			~36	39.1
	B$_2$				22.2				22.2
	A$_1$				19.0				18.9

[a] Values without references are from this work, b - broad, u - unresolved, s - shoulder, vw - very weak, m - Moulis *et al.* Ref. [20]

For example, the peaks at 240, 290, and 360 cm^{-1} downshift, respectively, to 232, 283, and 351 cm^{-1}. As expected, the ~3% shifts that we observe with ^{36}S substitution are roughly twice the fractional shifts observed in previous resonance Raman work with ^{34}S.[15] For an isolated ^{57}Fe–S harmonic oscillator, one expects 1.94% shifts for ^{32}S $\rightarrow$ ^{34}S, and 3.76% for ^{32}S $\rightarrow$ ^{36}S. Since the qualitative nature of the NRVS bands has already been discussed in reference to the IR and Raman data, we proceed to quantitative analysis using both DFT and empirical force fields.

DFT Analysis

In order to quantitatively interpret the NRVS spectra, and also to benchmark our ability to reproduce NRVS spectra from first principles, we undertook a normal mode analysis using density functional theory (DFT) calculations. The simulated and observed ^{57}Fe PVDOS spectra are compared in Fig. 2.
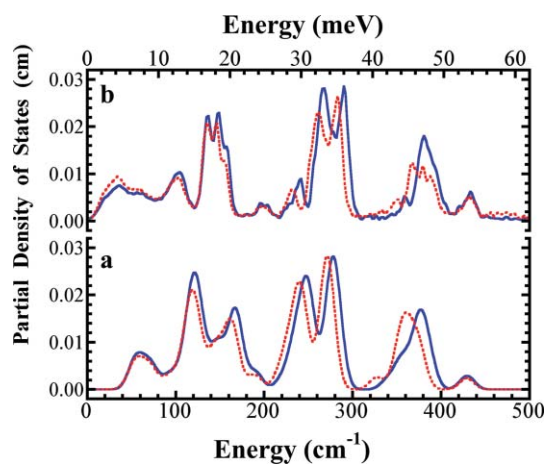
Fig. 2 (a) DFT simulation of ^{57}Fe PVDOS for $[^{57}Fe_4S_4(SPh)_4]^{2-}$ (blue line) and $[^{57}Fe_4{}^{36}S_4(SPh)_4]^{2-}$ (red dashed line); (b) Experimental ^{57}Fe PVDOS for $[^{57}Fe_4S_4(SPh)_4]^{2-}$ (blue line) and $[^{57}Fe_4{}^{36}S_4(SPh)_4]^{2-}$ (red dashed line).

The DFT simulations show good agreement with the experimental ^{57}Fe PVDOS spectra, especially in the high frequency region that contains the purest stretching motions. As shown in Table 3, the highest frequency peaks in the simulated PVDOS spectra (corresponding primarily to Fe–S^t and Fe–S^b stretches) are at 429 and 377 cm^{-1}, compared to observed intensity maxima at 433 and 381 cm^{-1}. For lower frequencies, the correspondence between DFT and observed results is not as close, but it is still within the expected range of error-peaks in the DFT simulation at 121, 167, 247 and 278 cm^{-1} probably correspond to observed maxima at 136, 149, 267 and 290 cm^{-1}. This assignment is supported by the close agreement between computed and observed frequency shifts upon ^{36}S substitution, as shown in Table 3. Overall, the DFT frequencies are systematically too low, by about 4 to 20 cm^{-1}. Studies of the dependence of such results on basis set and on the density functional chosen will be reported elsewhere. In addition to providing a reasonably good account of the frequencies, it is encouraging that that the DFT calculations also give a good account of relative intensities of various features in the PVDOS. This suggests that it may be possible to use both frequencies and intensities to compare observed and computed

Table 2 Comparison of UBFF force constants from [N(n-Bu)$_4$]$_2$[Fe$_4$S$_4$(SPh)$_4$] NRVS simulations *vs.* those derived from [Fe$_4$S$_4$(SCH$_2$Ph)$_4$]$^{2-}$ [15] and [Fe$_4$S$_4$(SMe)$_4$]$^{-}$ [14] clusters

| | K | K | K | K | H | H | H | H | F_{SSxy} | F_{SSz} | $F_{SS'}$ | $F_{SS'}$ | F_{FeFexy} | F_{FeFez} | F_{FeC} |
	Fe–S^t	Fe–S$_1^b$	Fe–S$_2^b$	S–C	S^b–Fe–S^b	S^t–Fe–S^b	Fe–S^b–Fe	Fe–S^t–C	S^b–S^b	S^b–S^b	S^t–S^b	S^t–S^b	Fe–Fe	Fe–Fe	Fe–C
This work	1.28	0.81	0.87	4.07	0.08	0.49	0.10	0.15	0.047	0.176	0.101	0.053	0.113	0.177	0.187
Spiro	1.4	0.95	1.13	3.05	0	0.25	0.17	0.25^a	0.08	0.1	0.05	0.042	0.19	0.23	0.12^a
Tuczek	1.28	0.98	1.06	2.82	0	0.42	0	0.33	0.12	0.12	0.064	0.05	0.26	0.22	0.06

Force constants from Spiro's 1994 JACS rubredoxin paper. Other force constants not used by Spiro/Tuczek: K_{CC} = 4.88; H_{SCC} = 0.70; H_{CCC} = 1.36.

^{a} Force constants from Spiro's 1994 JACS rubredoxin paper. Other force constants not used by Spiro/Tuczek paper.

Table 3 Isotope shift comparison for experimental, DFT calculation and UBFF calculation results

Experimental			DFT calculation			UBFF calculation		
^{32}S	^{36}S	Diff.	^{32}S	^{36}S	Diff.	^{32}S	^{36}S	Diff.
433[a]	433	0	429	429	0	431	431	0
381	367	14	377	361	16	379	367	12
290	283	7	278	271	7	288	286	2
267	261	6	247	240	7	268	261	7
149	145	4	167	162	5	152	152	0
136	135	1	121	119	2	137	135	2

[a] Units in cm^{-1}.

spectra in cases (such as proteins) where the structure is less well-characterized.

Urey–Bradley force field analysis

As an alternative approach to quantitative interpretation of the NRVS spectra, we undertook an empirical normal mode analysis using a Urey–Bradley force field. The results are summarized in Fig. 3 and Table 1. The vibrational spectra of 4Fe clusters in ferredoxins,[15] HiPIPs,[15] and $[Fe_4S_4X_4]^{2-}$ model complexes[14,15] have been extensively analyzed by this approach, and our interpretation relies on much of this body of work. We began with a simple tetrahedral $Fe_4S^b_4S^t_4$ model, in which the thiolate ligands are treated as point masses. The irreducible representation for the vibrational modes of this cluster is then:[15]

$$\Gamma_{vib} = 3A_1 + 3E + 2T_1 + 5T_2 \qquad (3)$$

The T_d model calculation (see ESI†) can serve as a starting point for describing the main features of the ^{57}Fe PVDOS spectra. In the T_d $Fe_4S^b_4S^t_4$ models, there are two A_1 Fe–S stretching modes, one of which mostly involves changing Fe–S^t distances, and the other mostly changing Fe–S^b distances. In alkylthiolates, the A_1 Fe–S^t stretching mode is found between 384 and 391 cm^{-1}, depending on the nature of the thiolate ligand,[14,15] while in ferredoxin and HiPIP samples, the A_1 Fe–S^t mode has been assigned at 395 and 397 cm^{-1}, respectively.[15] Although these modes are strong in the Raman spectra, it turns out they are nearly invisible in the NRVS-derived spectra. In the T_d $Fe_4S^b_4S^t_4$ simulation, we obtained an Fe–S^t A_1 mode at 385 and an Fe–S^b A_1 mode at 341 cm^{-1}. These are barely visible in the Fe PVDOS spectrum. In contrast, the third totally symmetric mode can be described as an Fe_4 'breathing' mode; this was reported at 165 cm^{-1} for the benzyl cube[15] and 152 cm^{-1} for the $[Fe_4S_4Cl_4]^{2-}$ cluster.[28] We assign the NRVS intensity at ~150 cm^{-1} to this mode; Moulis and coworkers observed a strong Raman band at 145 cm^{-1} in the solution spectrum of this compound.[20]

The asymmetric Fe–S stretching modes that descend from T_2 symmetry in a T_d model have been critical for past interpretations of $[Fe_4S_4(SR)_4]$ resonance Raman spectra. Czernuszewicz and coworkers assigned features in the benzyl cube spectra at 243/249 cm^{-1} and 359/367 cm^{-1} as derived from T_2 modes involving mostly Fe–S^b and Fe–S^t stretching, respectively.[15] The non-degeneracy was interpreted as the splitting of T_2 modes into E and B_2 modes in D_{2d} symmetry, and the absence of these splittings in the solution spectrum was taken as evidence for T_d symmetry in the liquid phase.[15] We also see this splitting of the T_2-derived modes— the ^{32}S NRVS spectrum has a peak at 241 cm^{-1} and a
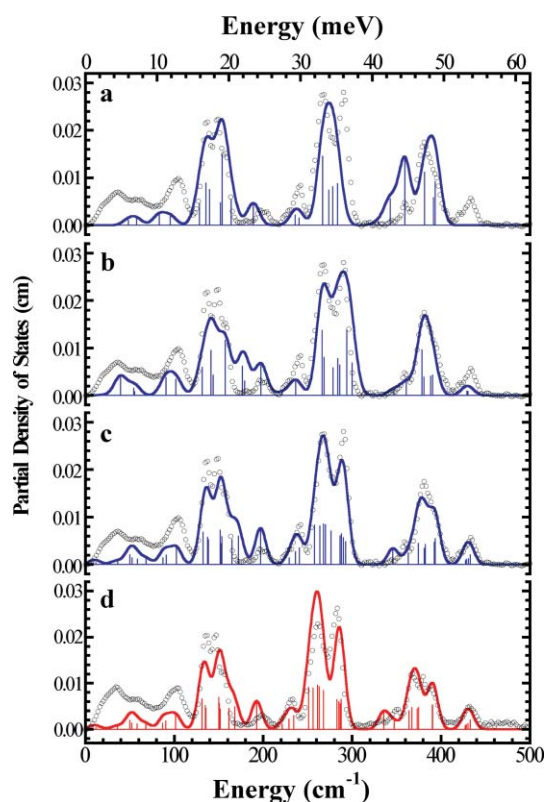

Fig. 3 Top to bottom: (a) ^{57}Fe PVDOS ($\cdots$) for $[(n\text{-}Bu)_4N]_2$-$[^{57}Fe_4S_4(SPh)_4]$ and UBFF simulation (solid blue line) for $^{57}Fe_4S_4S'_4$ model assuming D_{2d} symmetry; sticks represent intensities of discrete normal modes; (b) UBFF simulation (solid blue line) for $^{57}Fe_4S_4(SC_6)_4$ model assuming D_{2d} symmetry; (c) UBFF simulation (solid blue line) for $^{57}Fe_4S_4(SC_6)_4$ model without symmetry constraints; (d) UBFF simulation (solid red line) for $^{57}Fe_4{}^{36}S_4(SC_6)_4$ model without symmetry constraints and using same force field parameters as (c). The UBFF calculated PVDOS have been convoluted with a Voigt profile (50% Gaussian 8 cm^{-1} FWHM and 50% Lorentzian 8 cm^{-1} FWHM) to account for the monochromator and natural linewidths, respectively.

shoulder at 226 cm^{-1} that are reproduced in the low temperature IR spectrum. In other regions of the NRVS, accidental degeneracies and incomplete resolution conspire to hide most of these splittings. However, in the ^{36}S IR spectrum, the splitting of the T_2 Fe–S^t stretch into peaks at 367 and 350 cm^{-1} also demonstrates that the symmetry is lower than tetrahedral.

Of course, with extra degrees of freedom, a D_{2d} $Fe_4S^b_4S^t_4$ model yields a better simulation than the T_d model, but the 12-atom simulation has some clear limitations (Fig. 3); it does not reproduce the splitting in the 280 cm^{-1} region, it predicts two peaks around 380 cm^{-1} when only a broad band is observed, and it predicts nothing in the 435 cm^{-1} region previously assigned as the Fe–S^t stretch. Accordingly, we built a D_{2d} model with complete rings for the thiophenol ligands. With minor adjustment of parameters, inclusion of the rings resulted in much better agreement in the 435 cm^{-1} region, and resulted in reproduction of most features (frequencies as well as intensities) of the experimental Fe PVDOS spectra (Fig. 3). Predicted atomic motions of some important modes are shown in Fig. 4.

Since others have emphasized the unusual cluster symmetry in $[(n\text{-}Bu)_4N]_2[^{57}Fe_4S_4(SPh)_4]$, we also simulated the PVDOS both in
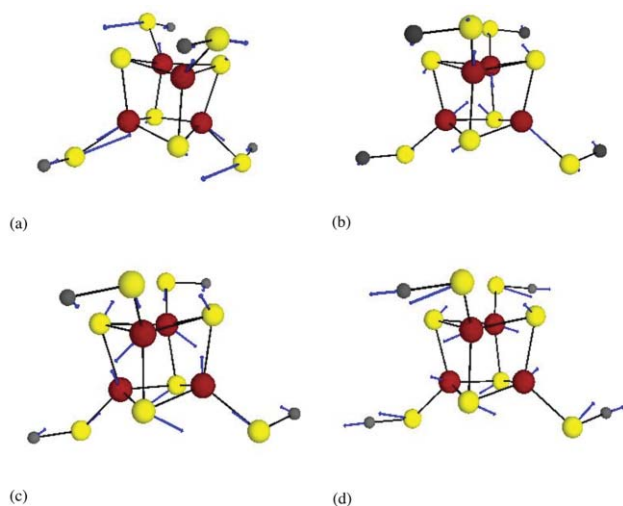
Fig. 4 Illustration of the atomic motions involved in different normal modes: (a) 430 cm^{-1}, (b) 294 cm^{-1}, (c) 144 cm^{-1} and (d) 55 cm^{-1}. Scheme 2 and this figure were created using MacMolPlot.[38]

C_2 symmetry and without symmetry (C_1). Compared with the D_{2d} calculation, the C_2 simulation did a better job of matching the 430 cm^{-1} intensity, as well as the intensity of the 150 cm^{-1} region (see ESI†), while the C_1 simulation yielded by far the best match to the amplitudes of all the Fe–S stretching modes (Fig. 3). As a final step in the refinement, we included NRVS data from [(n-Bu)$_4$N]$_2$[^{57}Fe$_4$^{36}S$_4$(SPh)$_4$] in the least squares optimization. We found that with small refinements, a self-consistent force field could be achieved that reproduced most of the spectral changes (Fig. 3). Finally, we note that even our model without symmetry constraints could not capture all the observed intensity below 100 cm^{-1}. Some of these low frequency modes presumably involve motion of the entire molecule, and additional work is needed on calculations that include the counterions.

Temperature-dependent spectra

A special feature of the [(n-Bu)$_4$N]$_2$[Fe$_4$S$_4$(SPh)$_4$] system is the structurally characterized phase transition at 243 K.[19] Spectra for [(n-Bu)$_4$N]$_2$[^{57}Fe$_4$S$_4$(SPh)$_4$] with natural abundance S and also with ^{36}S in the bridging locations, above and below this phase transition, are compared in Fig. 5. For the natural abundance S sample, the most striking change from below to above the phase transition is the loss of a peak at ∼400 cm^{-1}. The shoulder at 386 cm^{-1} in the ^{36}S-enriched spectrum also disappears above the phase transition. The low temperature features at 226 and 237 cm^{-1} shift to 223 and 232 cm^{-1} at 300 K. In the benzyl cube, a pair of E/B$_2$ components derived from the split T$_2$ Fe–S^b stretch was assigned at 243 and 249 cm^{-1}.[15] If the splitting of these features is taken as a measure of the deviation from T_d symmetry, the comparable splitting in both spectra is consistent with the cluster remaining distorted in both forms. Finally, the 145 cm^{-1} peak and 136 cm^{-1} shoulder in the low T IR collapse into a single weak band at ∼144 cm^{-1} in the room temperature IR.

We also recorded Raman spectra at room temperature with an FT Raman instrument using 10 640 Å excitation. Three strong peaks at 340, 264, and 150 cm^{-1} are observed; equal or close to three strong peaks at 340, 264, and 147 cm^{-1} seen in the 4880 Å
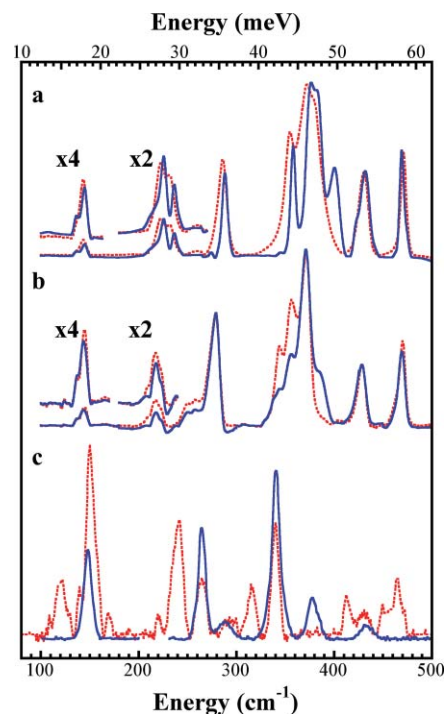
Fig. 5 Temperature effects on different normal modes. Top to bottom (a) [(n-Bu)$_4$N]$_2$[^{57}Fe$_4$S$_4$(SPh)$_4$] FT-IR at 300 K (red dashed line) and 100 K (blue line) and; (b) [(n-Bu)$_4$N]$_2$[^{57}Fe$_4$^{36}S$_4$(SPh)$_4$] FT-IR at 300 K (red dashed line) and 100 K (blue line) (c) [(n-Bu)$_4$N]$_2$[^{57}Fe$_4$S$_4$(SPh)$_4$] FT-Raman at 300 K (red dashed line) and resonance Raman at 77 K (blue line).

resonance Raman spectrum. As mentioned earlier, in the high energy range, a broad band at 433 cm^{-1} is seen both with 4880 Å excitation and in the room temperature FT Raman data, however, the latter also has peaks at 412 and 465 cm^{-1}.

Discussion

The low symmetry of the [Fe$_4$S$_4$(SPh)$_4$]$^{2-}$ cluster, the presence of multiple sites, and the structural phase transition at ∼240 K all conspire to complicate analysis the NRVS spectra. However, combining the NRVS with IR, Raman, and ^{36}S-substitution measurements has led to a self-consistent normal mode analysis. Since the vibrational spectra of numerous Fe$_4$S$_4$ model compounds and metalloproteins clusters have been analyzed before, we highlight areas where the new data help clarify some remaining issues.

Comparison of force fields

The force field that we have obtained agrees well with previous studies (Table 2).[14,15] With respect to the latter, the most significant differences are a weaker Fe–S^b (average 0.87 vs. 1.02 mdyne Å^{-1}), and a stronger S–C stretch force constant (4.1 vs. 2.8 mdyne Å^{-1}). All of the differences are consistent with the use of an aromatic thiolate ligand in the current work compared to aliphatic thiolates in previous studies, as well as a slightly more flexible cluster.

Observation of the 243 K phase transition

Excoffon and coworkers have described how the clusters in [(n-Bu)$_4$N]$_2$[Fe$_4$S$_4$(SPh)$_4$] become more distorted in the low

temperature form of the crystal structure, presumably *via* packing interactions between the counterion butyl groups and the cluster phenyl rings.[19] Our temperature-dependent IR data provide the first direct spectroscopic evidence for this transition. The most obvious change is the emergence of a resolved peak at 400 cm^{-1} upon cooling in the 'natural abundance' spectrum and a shoulder at 386 cm^{-1} in the ^{36}S-enriched spectrum.

Reassignment of the 435 cm^{-1} mode

The terminal Fe–S stretching modes for $[Fe_4S_4(Scys)_4]^{n-}$ and $[Fe_4S_4(Scys)_3X]^{n-}$ clusters in metalloproteins invariably fall below 400 cm^{-1};[15,29] thus the 435 cm^{-1} band observed in the $[Fe_4S_4(SPh)_4]^{2-}$ spectra is a clear outlier. One approach to generating cluster normal modes in the 435 cm^{-1} region involves raising the terminal Fe–S stretch force constant ($K_{Fe–S(t)}$) to a higher value than seen in rubredoxins or alkyl thiolate clusters; by adjusting this parameter modes that are primarily Fe–S stretch in character can be created at any desired frequency. Moulis and coworkers suggested that $K_{Fe–S(t)}$ for the thiophenolate cubane might be higher than normal because of delocalization of benzene π electrons toward the electrophilic $[Fe_4S_4]^{2+}$ core, and thus they proposed that the 435 cm^{-1} band was from a mode 'predominantly involving Fe–S^t stretching'.[20] However, the terminal Fe–S bond length is marginally (~0.01 Å) longer than in alkylthiolate cubanes; there is no structural indication of a stiffer bond.

Another problem with assigning a large fraction of Fe–S^t character to this mode is that it inevitably results in significant Fe motion, and a much larger NRVS signal than is actually observed. In an alternate approach, $K_{Fe–S(t)}$ can be left at conventional values, and the ligand force constants and/or geometry can be adjusted so that the Fe–S stretch couples with higher frequency ligand modes—the amount of Fe–S stretch character will depend on the degree of coupling. We have chosen this alternative interpretation, in which this mode involves primarily motion of the ligands. As illustrated in Fig. 4, in our analysis the 430 cm^{-1} mode has approximately 10% Fe–S^t character, and most of the motion involves the aromatic ring.

Nature of the ~150 cm^{-1} NRVS PVDOS intensity

A recent paper has reported a strong peak near 160 cm^{-1} in the NRVS of $[Et_4N]_2[Fe_4S_4(SCH_2Ph)_4]$.[30] Based on the observation that in 4Fe clusters, the ^{57}Fe nuclei are displaced from the molecular center of mass, it was proposed that the ~160 cm^{-1} intensity comes from 'rotational lattice modes' of the cubane anion.[30] However, our normal mode simulation points to a more conventional interpretation—the ~150 cm^{-1} region intensity in our spectra comes from modes that are primarily S–Fe–S and Fe–S–Fe bending in character (including A_1^{Fe} 'breathing') along with some ligand motion. These modes were observed in the early resonance Raman studies.[20] The assignment of this region to Fe 'breathing' modes is also supported by the DFT analysis. There does not seem to be any need for a lattice mode assignment in this region; the acoustic lattice modes are predicted to occur below 100 cm^{-1}. Both the empirical and DFT calculations do predict some optical modes below 100 cm^{-1} as well, these are attributed primarily to torsional motion of the cluster.

Summary

By combining NRVS spectra with complementary Raman and IR data, we have been able to observe nearly all the fundamental normal modes from 50–450 cm^{-1} of the Fe–S cluster in $[(n-Bu)_4N]_2[Fe_4S_4(SPh)_4]$. A DFT calculation using commonly employed functionals was found to produce good agreement with the Fe PVDOS frequencies and amplitudes. A Urey–Bradley force field for the $[Fe_4S_4(SPh)_4]^{2-}$ cluster was also derived that for the first time is accurate for both stretching and bending modes. The availability of spectra for the complex with ^{36}S-labeled bridging sulfides helped solidify assignments—modes with large isotope shifts had to have a significant component of bridging sulfide motion. As synchrotron sources continue to improve, the application of NRVS combined with resonance Raman and infrared spectroscopy should see many applications in bioinorganic chemistry.

Experimental

Sample preparation

$[(n-Bu)_4N]_2[^{57}Fe_4S_4(SPh)_4]$. This material was prepared by the following modification of published procedures.[31] Metallic ^{57}Fe (55.8 mg, 1.00 mmol) was loaded in a 3-neck round flask followed by addition of 150 mL concentrated HCl(aq.). The solution turned from a creamy color to pale yellow. The mixture was set to reflux at 120 °C for 36 h. The yellow solution was concentrated under reduced pressure till near dryness to give a slurry of brownish-yellow ^{57}FeCl$_3$. This material was transferred into the glove box where 100 ml of anhydrous THF were added. To the resulting suspension, sodium was added under vigorous stirring until no gas evolution was observed. The suspension was filtered, and the filtrate was reduced to dryness under reduced pressure. The resulting material was suspended in 3 ml of methanol. Sodium (92 mg, 4 mmol) was dissolved in 5 ml of methanol followed by the addition of benzenthiol (0.41 ml, 4 mmol). This solution was added drop-wise and under vigorous stirring to the suspension of the anhydrous ^{57}FeCl$_3$ and a deep brown suspension was evident after a few minutes. After 15 min, elemental sulfur (32 mg, 1 mmol) was added. The reaction mixture was stirred for 12 h at room temperature and was then filtered to a solution of Bu$_4$NI (0.277 g, 0.75 mmol) in 2 ml of MeOH. 75 mg (5.9% based on ^{57}Fe) of black crystals were isolated after one week and after washing with copious amounts of MeOH. Elemental ^{36}S (0.8% ^{32}S, 0.15% ^{34}S) was obtained from Isoflex, Inc. The corresponding ^{36}S-enriched sample was prepared by the same method described above, but reducing all quantities by a factor of 20. For NRVS measurements, the crystals were ground to a fine powder and loaded into 3 by 7 by 1 mm^3 (interior dimensions) Lucite cuvettes in an anaerobic N$_2$-containing glove box with an O$_2$ concentration <0.1 ppm.

Nuclear resonant vibrational spectroscopy

^{57}Fe NRVS spectra were recorded using published procedures[22] at beamline 3-ID at the Advanced Photon Source (APS).[32] Beamline 3-ID provided ~2.5 × 10^9 photons s^{-1} in 1 meV bandwidth at

14.4125 keV in a 0.5 high × 3 mm wide spot. The monochromators consisted of a water-cooled diamond Si(1,1,1) double crystal monochromator with 1.1 eV bandpass, followed by two Si channel-cut crystals, mounted on high precision rotation stages (Kohzu KTG-15AP) in a symmetry geometry.[33] The first channel-cut uses Si(4,0,0) reflections; the second uses the highest order possible reflection (10,6,4) at 14.4125 keV. During the NRVS measurements, the samples were maintained at cryogenic temperatures using liquid He. Since the cryostat temperature sensor was not directly in contact with the samples, the temperatures for individual spectra were calculated using the ratio of anti-Stokes to Stokes intensity according to: $S(-E) = S(E)\exp(-E/kT)$. Spectra were recorded between −20 meV and 80 meV in steps of 0.25 meV. Delayed nuclear fluorescence and Fe K fluorescence were recorded with a single avalanche photodiode.[34] Each scan took about 40 min, and all scans were added and normalized to the intensity of the incident beam. The spectra in the figures are averages of six scans for $[(n\text{-Bu})_4N]_2[^{57}Fe_4S_4(SPh)_4]$ and 12 scans for $[(n\text{-Bu})_4N]_2[^{57}Fe_4^{36}S_4(SPh)_4]$.

Raman spectroscopy

Resonance Raman spectra were recorded in a backscattering geometry from a KBr pellet of $[(n\text{-Bu})_4N]_2[Fe_4S_4(SPh)_4]$ immersed in a quartz liquid nitrogen Dewar at 77 K. The excitation source was a Coherent Innova-2 Ar$^+$/Kr$^+$ laser operated at 4880 Å, using a c.w. laser power of 35 mW. No sample radiation damage was observed. The spectra were recorded with a Spex model 1877 triple Raman spectrometer, using a liquid nitrogen cooled Spectrum One 594 CCD detector. The Raman spectra were calibrated using peaks at 218 cm^{-1} and 314 cm^{-1} in a room temperature CCl$_4$ sample. The entrance slit and slits 2/3 were set to 0.15 mm, yielding 6 cm^{-1} frequency resolution.

FT-IR spectroscopy

FT-IR samples were prepared as Nujol mulls in an anaerobic glove box and sealed in between polyethylene windows. Far-infrared absorption spectra were recorded using a Brücker IFS 66 v/S FT-IR spectrometer with a Mylar beamsplitter and a liquid He cooled Si bolometer. The sample chamber was continuously pumped to about 0.01 Torr to minimize the absorption by moisture vapor, and the energy resolution was 4 cm^{-1}. The cryogenic temperature experiments were performed with a liquid helium flow cryostat.

Density Functional Theory calculations

Spin-unrestricted broken-symmetry density functional calculations were carried out using the Jaguar[35] program, with the PWPW91 exchange and correlation functional[36] and the lacvp* basis set, which combines 6-31G* functions for H, C, N and O with a double-zeta effective core potential for Fe. Calculations began from the geometry of the $[Fe_4S_4(SPh)_4]^{2-}$ anion as found in the crystal structure; the initial symmetry was effectively maintained during the minimization and normal mode calculations, although no symmetry was imposed. Vibrational densities of states were computed using a Gaussian broadening of 8 cm^{-1}, weighting each mode by its e^2 value, as in eqn (2).

Empirical normal mode calculations

The normal mode calculations were carried out on T_d [Fe$_4$S$_4$S′$_4$], D_{2d} [Fe$_4$S$_4$S′$_4$], D_{2d} [Fe$_4$S$_4$(SPh)$_4$], C_2 [Fe$_4$S$_4$(SPh)$_4$], and C_1 [Fe$_4$S$_4$(SPh)$_4$] (no symmetry) models by using Wilson's GF matrix method and a Urey–Bradley force field. The coordinates for [N(n-Bu)$_4$]$_2$[Fe$_4$S$_4$(SPh)$_4$] were taken from the low temperature X-ray crystal structure.[19] The calculations used the program 'Atoms' to build the molecular models and a special modification of program 'Vibratz' to calculate the normal modes and NRVS spectra.[37]

References

1 M. K. Johnson, Iron-sulfur proteins in *Encyclopedia of Inorganic Chemistry*, ed. R. B. King, Wiley, Chichester, 1994, pp. 1896-1915.
2 R. Kummerle, P. Kyritsis, J. Gaillard and J. M. Moulis, Electron transfer properties of iron-sulfur proteins, *J. Inorg. Biochem.*, 2000, **79**, 83–91.
3 P. J. Kiley and H. Beinert, Role of Fe–S proteins in sensing and regulation in bacteria, *Curr. Opin. Microbiol.*, 2003, **6**, 181–185.
4 M. C. Corbett, Y. Hu, F. Naderi, M. W. Ribbe, B. Hedman and K. O. Hodgson, Comparison of iron–molybdenum cofactor-deficient nitrogenase MoFe proteins by X-ray absorption spectroscopy: implications for P-cluster biosynthesis, *J. Biol. Chem.*, 2004, **279**, 28276–28282.
5 J. Cheek and J. B. Broderick, Adenosylmethionine-dependent iron-sulfur enzymes: versatile clusters in a new radical role, *J. Biol. Inorg. Chem.*, 2001, **6**, 209–226.
6 D. C. Rees, Great metalloclusters in enzymology, *Annu. Rev. Biochem.*, 2002, **71**, 221–246.
7 C. L. Drennan and J. W. Peters, Surprising cofactors in metalloenzymes, *Curr. Opin. Struct. Biol.*, 2003, **13**, 220–226.
8 W. M. Fitch and M. Bruschi, The evolution of prokaryotic ferredoxins—with a general method correcting for unobserved substitutions in less branched lineages, *Mol. Biol. Evol.*, 1987, **4**, 381–394.
9 W. Martin and M. J. Russell, On the origins of cells: a hypothesis for the evolutionary transitions from abiotic geochemistry to chemoautotrophic prokaryotes, and from prokaryotes to nucleated cells, *Philos. Trans. R. Soc. London, Ser. B*, 2003, **358**, 59–83.
10 L. Liu, T. Nogi, M. Kobayashi, T. Nozawa and K. Miki, Ultrahigh-resolution structure of high-potential iron-sulfur protein from *Thermochromatium tepidum*, *Acta Crystallogr., Sect. D*, 2002, **D58**, 1085–1091.
11 K. Fukuyama, T. Okada, Y. Kakuta and Y. Takahashi, Atomic resolution structures of oxidized [4Fe–4S] ferredoxin from *Bacillus thermoproteolyticus* in two crystal forms: systematic distortion of [4Fe–4S] cluster in the protein, *J. Mol. Biol.*, 2002, **315**, 1155–1166.
12 Z. Dauter, K. S. Wilson, L. C. Sieker, J. Meyer and J. M. Moulis, Atomic resolution (0.94 A) structure of *Clostridium acidurici* ferredoxin. Detailed geometry of [4Fe–4S] clusters in a protein, *Biochemistry*, 1997, **36**, 16065–16073.
13 P. V. Rao and R. H. Holm, Synthetic Analogues of the Active Sites of Iron–Sulfur Proteins, *Chem. Rev.*, 2004, **104**, 527–559.
14 A. Kern, C. Nather, F. Studt and F. Tuczek, Application of a universal force field to mixed Fe/Mo–S/Se cubane and heterocubane clusters. 1. Substitution of sulfur by selenium in the series [Fe$_4$X$_4$(YCH$_{34}$)$_2$]$^-$; X = S/Se and Y = S/Se, *Inorg. Chem.*, 2004, **43**, 5003–5010.

15 R. S. Czernuszewicz, K. A. Macor, M. K. Johnson, A. Gewirth and T. G. Spiro, Vibrational Mode Structure and Symmetry in Proteins and Analogues Containing Fe_4S_4 Clusters: Resonance Raman Evidence for Different Degrees of Distortion in HiPIP and Ferredoxin, *J. Am. Chem. Soc.*, 1987, **109**, 7178–7187.

16 L. Que, Jr., M. A. Bobrik, J. A. Ibers and R. H. Holm, Synthetic analogs of the active sites of iron-sulfur proteins. VII. Ligand substitution reactions of the tetranuclear clusters $(Fe_4S_4(SR)_4)^{2-}$ and the structure of $((CH3)_4N)_2(Fe_4S_4(SC_6H_{54}$, *J. Am. Chem. Soc.*, 1974, **96**, 4168–4178.

17 J. Gloux, P. Gloux, H. Hendriks and G. Rius, EPR Study of the $[Fe_4S_4]^+$ and $[Fe_4S_4]^{3+}$ States in γ-Irradiated Crystals of $(Bu_4N)_2[Fe_4S_4(SPh)_4]$. *g*-Tensors in Relation to the Geometry of the 4Fe–4S Core, *J. Am. Chem. Soc.*, 1987, **109**, 3220–3224.

18 G. Lin, H. Zhang, S.-Z. Hu and T. C. W. Mak, Structure of bis(tetra-n-butylammonium) 1,2,3;1,2,4;1,3,4;2,3,4-tetra-*m*-sulfido-tetrakis[(benzenethiolato)iron], *Acta Crystallogr.*, 1987, **43**, 352–353.

19 P. Excoffon, J. Laugier and B. Lamotte, Influence of a Phase Transition in the Solid State on the Structure of a Synthetic Iron-Sulfur Cubane, *Inorg. Chem.*, 1991, **30**, 3075–3081.

20 J.-M. Moulis, J. Meyer and M. Lutz, $[4Fe–4S]^{2+}$ (X = Sulfur, Selenium) Clusters in *Clostridium pasteurianum* Ferredoxin and in Synthetic Analogues: Structural Data from Resonance Raman Spectroscopy, *Biochemistry*, 1984, **23**, 6605–6613.

21 E. Alp, W. Sturhahn, T. S. Toellner, J. Zhao, M. Hu and D. E. Brown, Vibrational Dynamics Studies by Nuclear Resonant Inelastic X-Ray Scattering, *Hyperfine Interact.*, 2002, **144/145**, 3–20.

22 W. Sturhahn, Nuclear resonant spectroscopy, *J. Phys.: Condens. Matter*, 2004, **16**, S497–S530.

23 B. M. Leu, M. Z. Zgierski, G. R. A. Wyllie, W. R. Scheidt, W. Sturhahn, E. E. Alp, S. M. Durbin and J. T. Sage, Quantitative Vibrational Dynamics of Iron in Nitrosyl Porphyrins, *J. Am. Chem. Soc.*, 2004, **126**, 4211–4227.

24 W. Sturhahn, T. S. Toellner, E. E. Alp, X. Zhang, M. Ando, Y. Yoda, S. Kikuta, M. Seto, C. W. Kimball and B. Dabrowski, Phonon Density of States Measured by Inelastic Nuclear Resonant Scattering, *Phys. Rev. Lett.*, 1995, **74**, 3832–3835.

25 J. T. Sage, C. Paxson, G. R. A. Wyllie, W. Sturhahn, S. M. Durbin, P. M. Champion, E. E. Alp and W. R. Scheidt, Nuclear resonance vibrational spectroscopy of a protein active-site mimic, *J. Phys.: Condens. Matter*, 2001, **13**, 7707–7722.

26 W. Sturhahn, CONUSS and PHOENIX: evaluation of nuclear resonant scattering data, *Hyperfine Interact.*, 2000, **125**, 149–172.

27 K. Nakamoto, *Infrared and Raman Spectra of Inorganic and Coordination Compounds*, 5th edn, Wiley-Interscience, New York, 1997.

28 A. Kern, C. Näther and F. Tuczek, Application of a Universal Force Field to Mixed Fe/Mo–S/Se Cubane and Heterocubane Clusters. 2. Substitution of Iron by Molybenum in $Fe_4(S/Se)_4$ Clusters with Terminal Halide and Thiolate Ligands, *Inorg. Chem.*, 2004, **43**, 5011–5020.

29 P. S. Brereton, R. E. Duderstadt, C. R. Staples, M. K. Johnson and M. W. W. Adams, Effect of Serinate Ligation at Each of the Iron Sites of the $[Fe_4S_4]$ Cluster of *Pyrococcus furiosus* Ferredoxin on the Redox, Spectroscopic, and Biological Properties, *Biochemistry*, 1999, **38**, 10594–10605.

30 V. S. Oganesyan, J. E. Barclay, S. M. Hardy, D. J. Evans, C. J. Pickett and U. A. Jayasooriya, Nuclear inelastic scattering spectroscopy of iron-sulfur cubane compounds, *Chem. Commun.*, 2004, 214–215.

31 Y. Do, E. D. Simhon and R. H. Holm, Improved Syntheses of $[Fe_2S_2Cl_4]^{2-}$ and $[Fe_2OCl_6]^{2-}$ and Oxo Sulfido Ligand Substitution by use of Silylsulfide Reagents, *Inorg. Chem.*, 1983, **22**, 3809–3812.

32 T. Toellner, Monochromatization of synchrotron radiation for nuclear resonant scattering experiments, *Hyperfine Interact.*, 2000, **125**, 3–28.

33 T. S. Toellner, M. Y. Hu, W. Sturhahn, K. Quast and E. E. Alp, Inelastic nuclear scattering with sub-meV resolution, *Appl. Phys. Lett.*, 1997, **71**, 2112–2114.

34 S. Kishimoto, Y. Yoda, M. Seto, S. Kitao, Y. Kobayashi, R. Haruki and T. Harami, *Nucl. Instrum. Methods Phys. Res. A*, 2003, 193–196.

35 Jaguar, Schrödinger Software.

36 J. P. Perdew, J. A. Chevary, S. H. Vosko, K. A. Jackson, M. R. Pederson, D. J. Singh and C. Fiolhais, Atoms, Molecules, Solids, and Surfaces-Applications of the Generalized Gradient Approximation for Exchange and Correlation, *Phys. Rev. B*, 1992, **46**, 6671–6687.

37 E. Dowty, Fully automated microcomputer calculationof vibrational spectra, *Phys. Chem. Minerals*, 1987, **14**, 67–79.

38 B. M. Mode and M. S. J. Gordon, MacMolPlt: a graphical user interface for GAMESS, *J. Mol. Graphics Mod.*, 1998, **16**, 133–138.